Effect of metallurgical evolution during post-weld aging treatment on localized corrosion of resistance spot welding joints of A286 superalloy

Pilar De Tiedra[a], Óscar Martín[b,*], Manuel San-Juan[b]

[a] Ciencia de los Materiales e Ingeniería Metalúrgica, Departamento CMeIM/EGI/ICGF/IM/IPF, Universidad de Valladolid, Escuela de Ingenierías Industriales, Paseo del Cauce 59, Valladolid 47011, Spain.

[b] Ingeniería de los Procesos de Fabricación, Departamento CMeIM/EGI/ICGF/IM/IPF, Universidad de Valladolid, Escuela de Ingenierías Industriales, Paseo del Cauce 59, Valladolid 47011, Spain.

[*] Corresponding author. Ph.: +34-983185037, Fax: +34-983423310, E-mail: oml@eii.uva.es (Ó. Martín)

Abstract

The combined effect of resistance spot welding and precipitation hardening on the localized corrosion of A286 superalloy is studied. The specimens tested by DLEPR were welded in the solution treated condition, and then subjected to different precipitation hardening treatments. For both base metal and weld nugget, the maximum localized corrosion is reached when η phase is clearly observable. The fact that the localized corrosion resistance of weld nugget is different from that shown by base metal may be explained by the segregation of Ni and Ti towards the interdendritic region of weld nugget (studied by using SEM/EDX analysis).

Keywords: Resistance spot welding; A286 superalloy; Precipitation hardening; Gamma prime phase; Eta phase; DLEPR; SEM; Fusion zone.

1 Introduction

A286 iron-nickel superalloy is a precipitation-hardenable austenitic stainless steel which is widely used in gas turbine industry because of its good thermal resistance, superior mechanical properties and ease of fabrication [1], with, as pointed out by Mouritz [2], several advantages over nickel or cobalt superalloys such as a lower thermal expansion at high temperature, which is an important property for engine components requiring closely controlled clearances between rotating parts, and a lower cost. A286 superalloy is also utilized in cryogenic devices [3], in nonmagnetic oil well equipments [3], and in the nuclear industry [4,5].

A286 superalloy is strengthened by the precipitation of the ordered fcc gamma prime (γ') $Ni_3(Al,Ti)$ phase [6–9], which, as indicated by Zhao et al. [10], is coherent with the matrix. The γ' phase is unstable [11] and thus, after a sufficiently long aging treatment at sufficiently high temperature, dissolves to form the hcp eta (η) Ni_3Ti phase that, at aging temperatures between 600 and 850 °C [12], precipitates at grain boundary by cellular reaction [13]. The cellular η phase precipitation at grain boundary may be detrimental to the mechanical properties because degrades the creep behaviour [14], causes the increase in intergranular fracture in the tensile test [15], aggravates the hydrogen embrittlement sensitivity [16], and induces the decrease in fatigue life [17].

A286 superalloy is a difficult material to weld because of its high susceptibility to hot cracking in the fusion zone [18,19]; this solidification cracking is caused by the formation of a low melting point phase at the grain boundaries, which is produced by the segregation of Ti and other solutes during the last stages of solidification [19–22]. Resistance spot welding (RSW) is one of the primary methods in the automotive industry for joining sheet metals [23,24], because, as mentioned by Martín et al. [25,26], its high speed and adaptability for automation render it suitable for mass production. RSW of stainless steel sheets is also widely used, as stated by Kianersi at al. [27], in transportation vessels, kitchen furniture and utensils and building applications. In addition to this, the possibility of using stainless steels in structural automotive was studied by a next generation vehicle (NGV) programme [28]. Although the general practice in welding superalloys is to employ a weaker, more ductile austenitic filler metal than the base metal to minimize weld cracking, when the maximum joint strength is required, filler metal of base metal composition is used [29]. Thus, RSW, which is an autogenous welding process (i.e., without filler metal), is a promising method for welding A286 superalloy [19].

The influence of precipitation hardening on the corrosion behaviour of A286 superalloy has been studied in previous works [30,31] where it was concluded that γ' and η precipitates may cause the passive layer that forms on them to become more unstable. On the other hand, as indicated by Martín et al. [19], in the weld nugget of the RSW joint, which is formed from the solidification of the molten metal [32,33], the interdendritic region is enriched in Ni and Ti. Thus, the combined effect of RSW, which gives rise to the segregation of Ni and Ti in the weld nugget (fusion zone), and a subsequent precipitation hardening treatment, which causes the

precipitation of γ' and η phases (Ni and Ti-rich phases), may have influence on the localized corrosion of A286 superalloy.

Electrochemical potentiokinetic reactivation (EPR) and double loop electrochemical potentiokinetic reactivation (DLEPR) are quasi non-destructive tests which are much quicker, more sensitive and more accurate than the conventional corrosion tests [34] and that are widely used to evaluate the localized corrosion in stainless steels [35–37]. Since EPRDL measures electrochemical parameters on comparative basis between activation and reactivation scans, the results are not so sensitive to test conditions and to surface state of the specimens [38,39]. A lacquer coating technique was used for selecting the different uncovered areas to study but, since some problems related to crevice corrosion may occur [36], and considering that the results of EPRDL are not so sensitive to surface state as those of EPR, the DLEPR technique was chosen in the present work.

The present work aims to study of the effect of metallurgical evolution during post-weld aging treatment on localized corrosion of resistance spot welding joints by using DLEPR test.

2 Experimental Procedure

2.1 Materials

The chemical composition of the A286 superalloy sheets welded by RSW is shown in Table 1. The sheet thickness was 1 mm.

Table 1. Chemical composition of A286 superalloy sheets (wt %).

C	Si	Mn	P	S	Cr	Mo	Ni	V	Ti	Al	B	Fe
0.032	0.50	1.24	0.011	<0.0003	14.98	1.18	24.74	0.29	2.30	0.16	0.0046	Bal.

2.2 Scanning Electron Microscope (SEM)

SEM micrographs were obtained after mechanical polishing and electrolytic etching with etchant No. 83 according to ASTM E407-07e1 (at 6 V for 60 s in a solution of 10 g CrO_3 in 100 ml water) [40]. SEM observations were conducted on a FEI-Quanta 200FEG operating at 20 kV and equipped with an energy dispersive X-ray analysis (EDX) to determine the chemical composition in the weld nugget.

2.3 Specimens tested by DLEPR

Specimens tested by DLEPR were firstly welded, as indicated by Hoppin and Yount [29], by RSW in the solution treated condition (solution treatment was carried out at 927 °C for 0.25 h and followed by water quenching), and then subjected to different precipitation hardening treatments (see Table 2). According to Table 2, there were 7 different specimens.

The A286 superalloy sheets were welded with a single-phase alternating current (AC) 50 Hz equipment by using water-cooled truncated cone RWMA Group A Class 2 electrodes [41] with 16 mm body diameter and 5 mm face diameter. The controlled parameters in the RSW process of the tensile shear test specimens were, according to Aslanlar [42]: welding time (WT), welding current (WC), and electrode force (EF). The values of the welding parameters were fixed at WT = 0.36 s, WC = 6 kA and EF = 2300 N [20].

Table 2. Specimens tested by DLEPR. Specimen No. 0 was subjected to no precipitation hardening treatment, i.e. it was in the solution treated condition. Each of different precipitation hardening treatments was followed by air cooling.

Solution treated condition		RSW process	Precipitation hardening		Specimen No.
Temperature (°C)	Time (h)		Temperature (°C)	Time (h)	
927	0.25	WT = 0.36 s WC = 6 kA EF = 2300 N		N/A	N/A	0
			720	0.5	1
				10	2
				25	3
				50	4
				100	5
				200	6

There are two distinct areas in each of the seven specimens tested by DLEPR (Fig. 1): (i) the base metal; and (ii) the weld nugget, which is formed from the solidification of the molten metal and, consequently, has an as-cast dendritic microstructure [19,32,33].
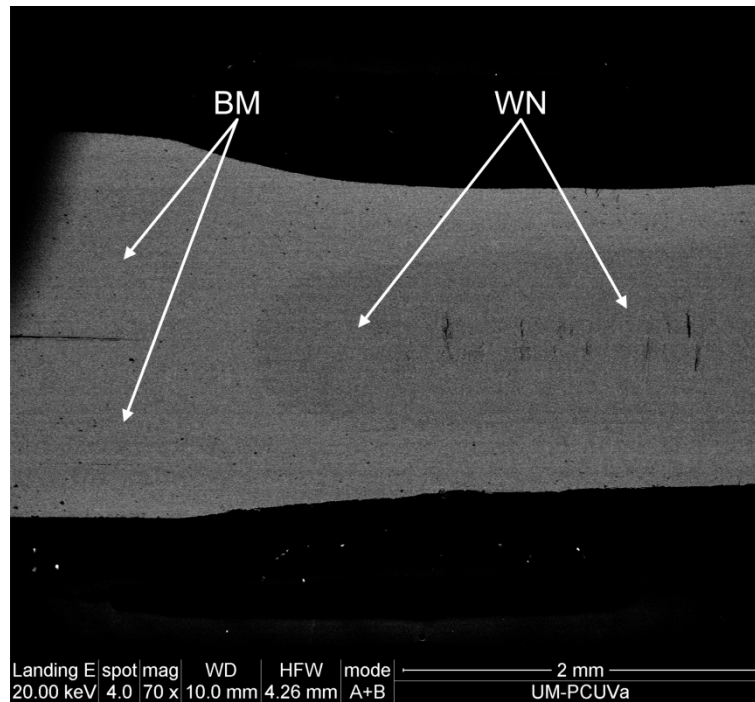
Fig. 1. SEM micrograph of a cross sectioned specimen tested by DLEPR (No. 4) that shows the weld nugget (WN) and the base metal (BM). Electrolytic etching with etchant No. 83 according to ASTM E407-07 [40].

2.4 DLEPR test

The large-scale electrochemical cell used for performing the DLEPR test had two high-purity carbon auxiliary (counter) electrodes and a saturated calomel electrode (SCE) positioned in front of the specimen at a distance of 4 mm [35]. The electrolyte was 0.5 M H_2SO_4 + 0.01 M KSCN and the test temperature was 30 °C ± 1. The three stages of the test were: (i) a 5 min delay at open circuit (OC) potential; (ii) an anodic polarization scan from 50 mV below VOC to 200 mV(SCE) at a scan rate of 1.67 mV/s; (iii) a cathodic reactivation scan from 200 mV(SCE) to VOC at the same scan rate. The ratio between charges in the reactivation scan Q_r (C/cm^2) and in the activation scan Q_a (C/cm^2), Q_r/Q_a (%), was used to measure the localized corrosion [35,43]: the greater the Q_r/Qa ratio, the higher the localized corrosion.

A lacquer coating was used to select an uncovered area [36,44], where performing the DLEPR test, and thus, three different DLEPR tests were performed on each of the seven specimens (Fig. 2): (i) DLEPR test performed on the entire specimen (without lacquer coating); (ii) DLEPR test performed on the base metal; and (iii) DLEPR test performed on the weld nugget.
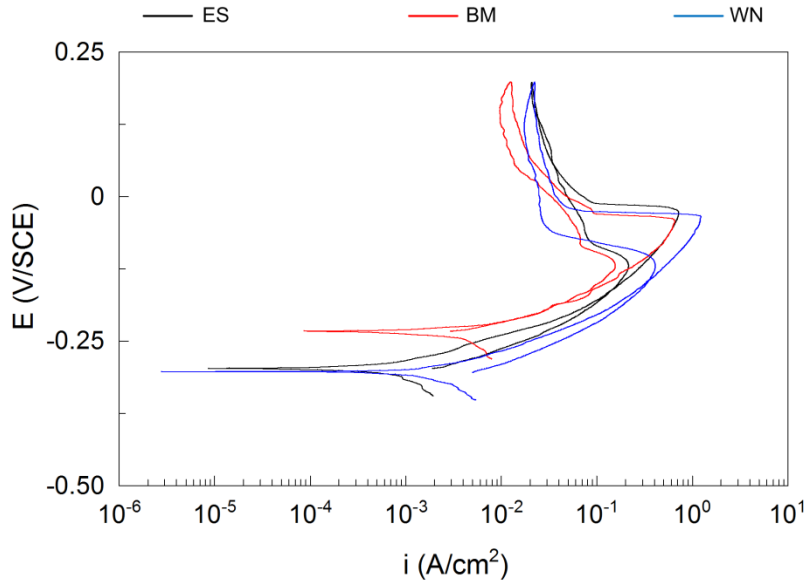
Fig. 2. Curves obtained from the three different DLEPR tests performed on the entire specimen (ES), on the base metal (BM) and on the weld nugget (WN) of the specimen No. 4.

The heat-affected zone was not specifically studied, but was studied together with the base metal, because it was so narrow [45] that it was impossible to isolate it with the methodology used. In any case, no significant microstructural changes were observed, compared with the base metal, in the zone adjacent to the weld nugget (Fig. 3), except a slightly greater continuity of the attack in grain boundary (Fig. 4).
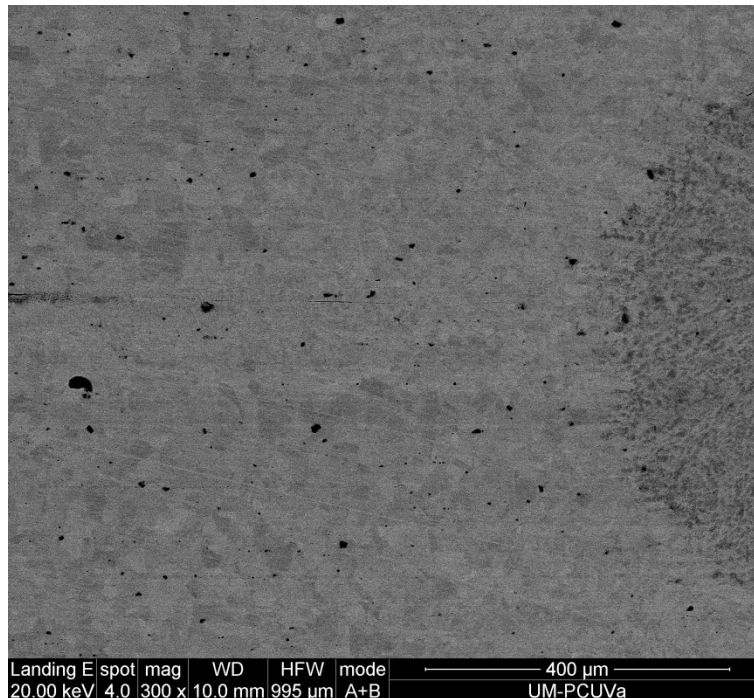

Fig. 3. SEM micrograph that shows the base metal and the zone adjacent to the weld nugget (specimen No. 4). Electrolytic etching with etchant No. 83 according to ASTM E407-07 [40].

6

Fig. 4. Optical micrograph that shows the base metal and the zone adjacent to the weld nugget (specimen No. 6). Micrograph taken after DLEPR test.

3 Results and discussion

As shown in Fig. 5, the aging time at which the maximum localized corrosion is reached is 25 h for the base metal and 50 h for the weld nugget. The SEM examination shows that, for both the base metal and the weld nugget, the maximum localized corrosion is reached at the aging time from which the η phase is clearly observable: at 25 h for the base metal (Figs. 6 and 7) [30,31] and at 50 h for the weld nugget (Figs. 8 and 9) [19]. The localized corrosion for the entire specimen: (i) takes an intermediate value between those of the base metal and weld nugget; and (ii) reaches its highest values at the aging times from which the η phase is clearly observable in the base metal (25 h) and in the weld nugget (50 h).

Both in the base metal and in the weld nugget, before the η phase is clearly observable, the localized corrosion increases as the aging time increases, i.e., since γ' phase is precipitated early in aging and subsequent aging is basically a coarsening process [8], as γ' precipitates grow. This result agrees with that obtained by Martín et al. [31], and it is consistent with the fact that, as indicated by Číhal and Štefec [46], γ' precipitate distributed throughout the matrix may cause discontinuities in the passive layer.

The complex effect of η phase on the localized corrosion may be explained by the fact that the η phase precipitation at grain boundary promotes the localized corrosion at grain boundary [31] on the one hand, whilst on the other, the η phase indirectly improves the localized corrosion resistance because it grows at the expense of γ' phase [10,30,31,47–50].
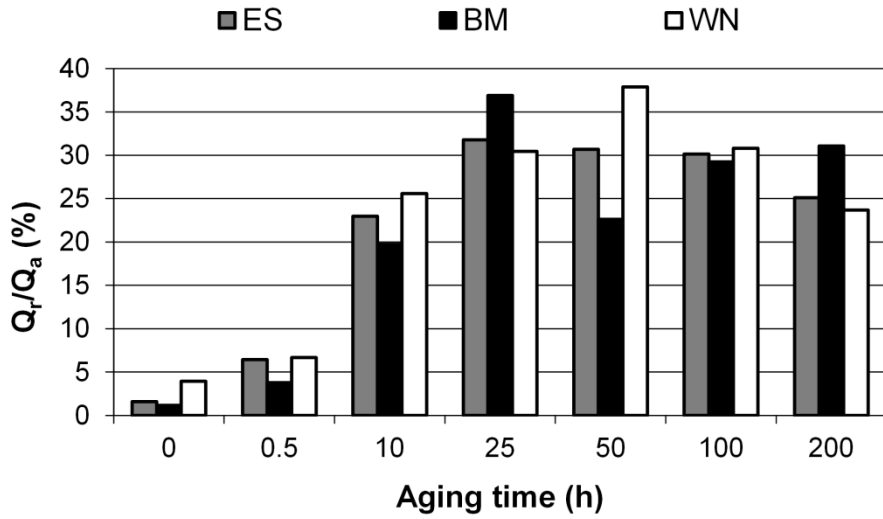
Fig. 5. Ratio between charges in the reactivation scan Q_r (C/cm^2) and in the activation scan Q_a (C/cm^2), Q_r/Q_a (%), obtained from the three different DLEPR tests performed on the entire specimen (ES), on the base metal (BM) and on the weld nugget (WN) of each of the seven specimens shown in Table 2. Specimen No. 0 was in the solution treated condition, i.e. it was subjected to no precipitation hardening treatment and then the corresponding aging time was considered as 0 h.
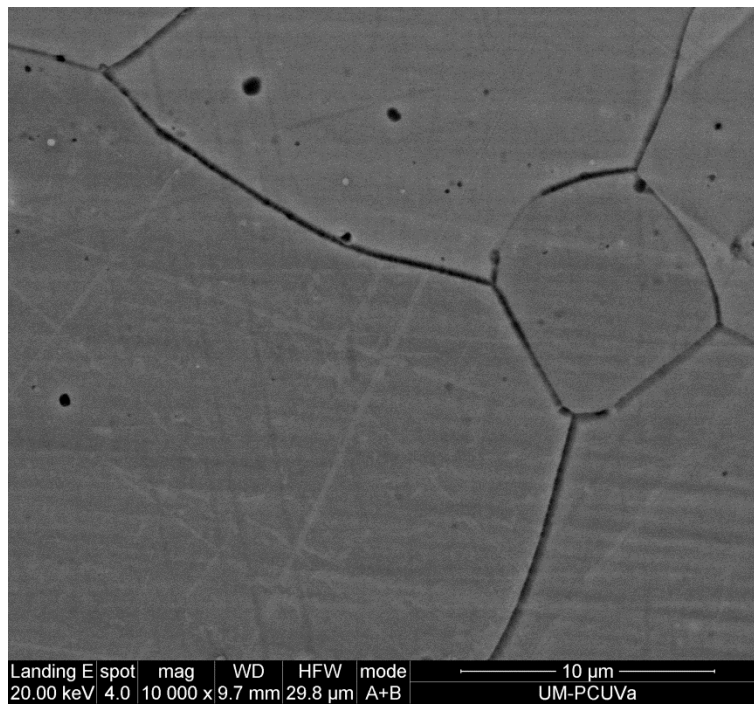

Fig. 6. SEM micrograph of the base metal of the specimen No. 2 where the η phase cannot be clearly observed. Electrolytic etching with etchant No. 83 according to ASTM E407-07 [40].
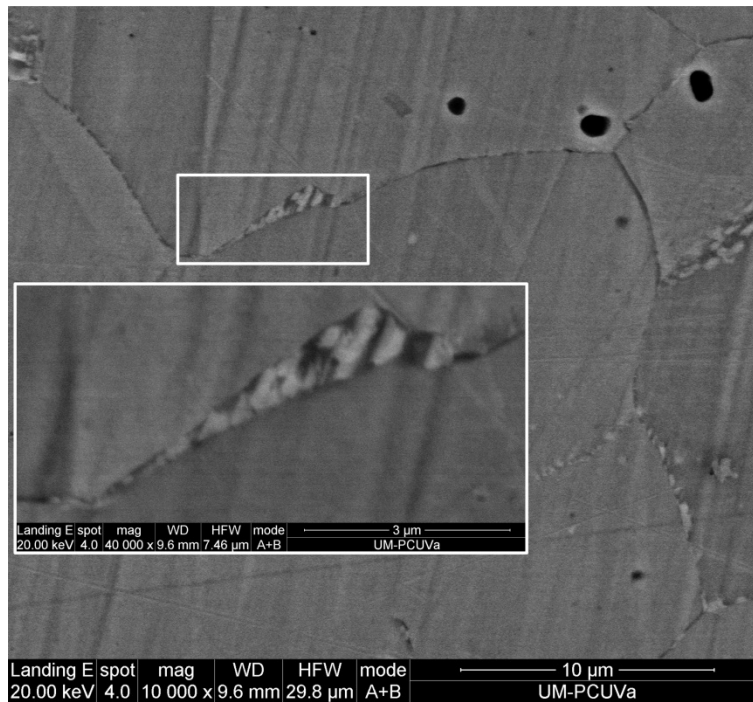
Fig. 7. SEM micrograph of the base metal of the specimen No. 3 that shows the η phase precipitation at grain boundary. The inset provides a higher magnification image of the η phase whose lamellar structure is clearly observable. Electrolytic etching with etchant No. 83 according to ASTM E407-07 [40].
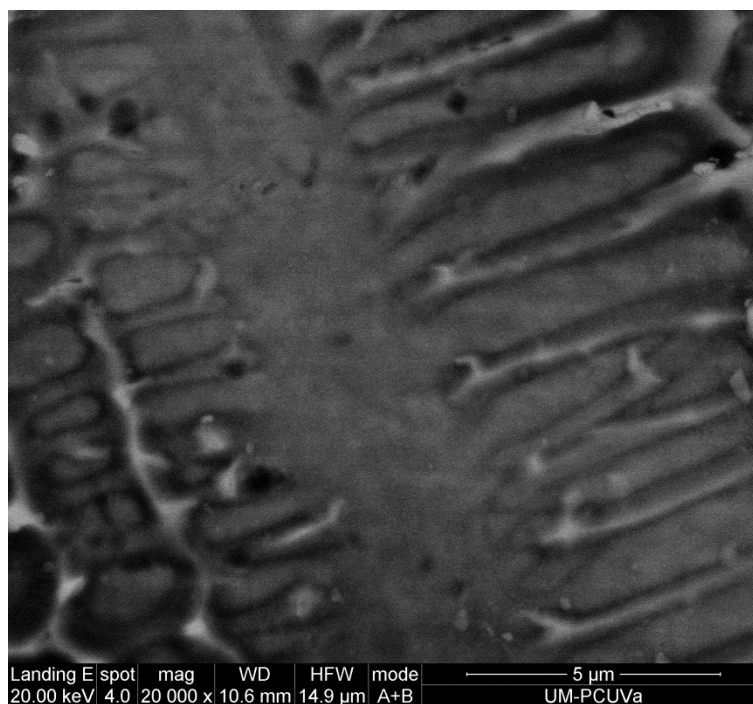

Fig. 8. SEM micrograph of the weld nugget of the specimen No. 3 where the η phase cannot be clearly observed. Electrolytic etching with etchant No. 83 according to ASTM E407-07 [40].
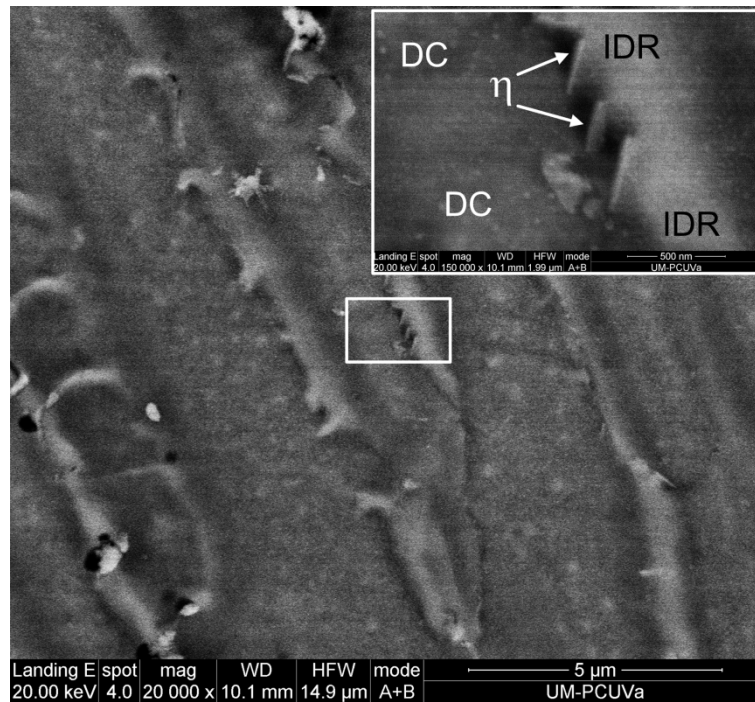
Fig. 9. SEM micrograph of the weld nugget of the specimen No. 4 that shows the η phase precipitation at the interface between dendrite core (DC) and interdendritic region (IDR) [19]. The inset provides a higher magnification image of the η phase whose lamellar structure is clearly observable. Electrolytic etching with etchant No. 83 according to ASTM E407-07 [40].

The fact that, as seen in Fig. 5, the localized corrosion resistance of the weld nugget is different from that shown by the base metal may be explained by the fact that, as explained in [20–22], the interdendritic regions of the weld nugget microstructure are enriched in certain solute elements whose segregation takes place during the solidification. This phenomenon was studied by SEM/EDX analysis in the interdendritic region and in the dendrite core of the weld nugget (Figs. 10 to 12). The main results of this analysis are shown in Tables 3 and 4.

As shown in Table 3, the interdendritic region of the weld nugget is, according to the partition coefficient k_{IDR} estimated as the ratio between the interdendritic region composition and the nominal composition of the alloy, enriched in Ni and Ti and depleted in Fe and Cr; this result agrees with that obtained by Brooks and Krenzer [21].

As shown in Table 4, the dendrite core of the weld nugget is, according to the partition coefficient k_{DC} estimated as the ratio between the dendrite core composition and the nominal composition of the alloy, depleted in Ni and Ti [18] and slightly enriched in Fe and Cr; this result is consistent with that obtained in the interdendritic region.
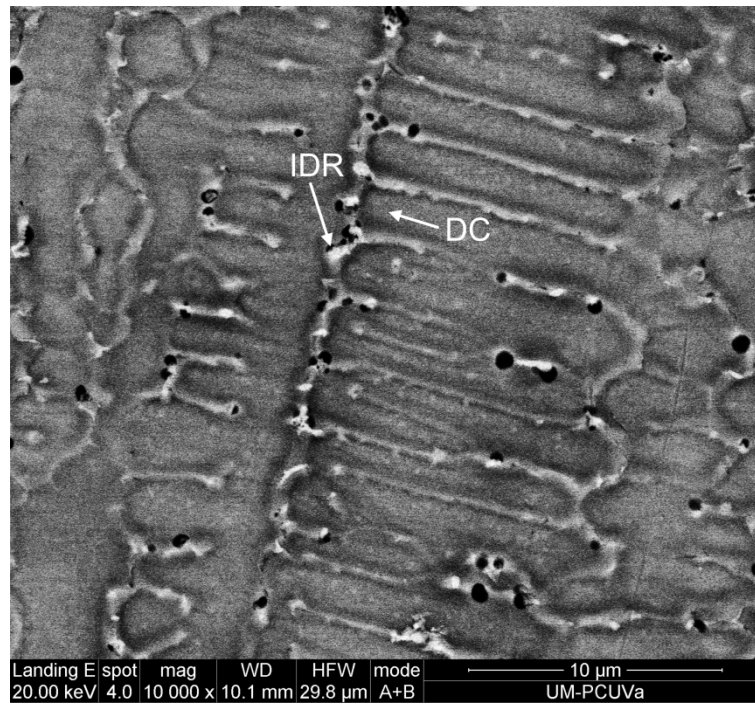
Fig. 10. SEM micrograph of the weld nugget of the specimen No. 4. The arrows indicate where the SEM/EDX analyses were performed, both on the interdendritic region (IDR) and on the dendrite core (DC). Electrolytic etching with etchant No. 83 according to ASTM E407-07 [40].
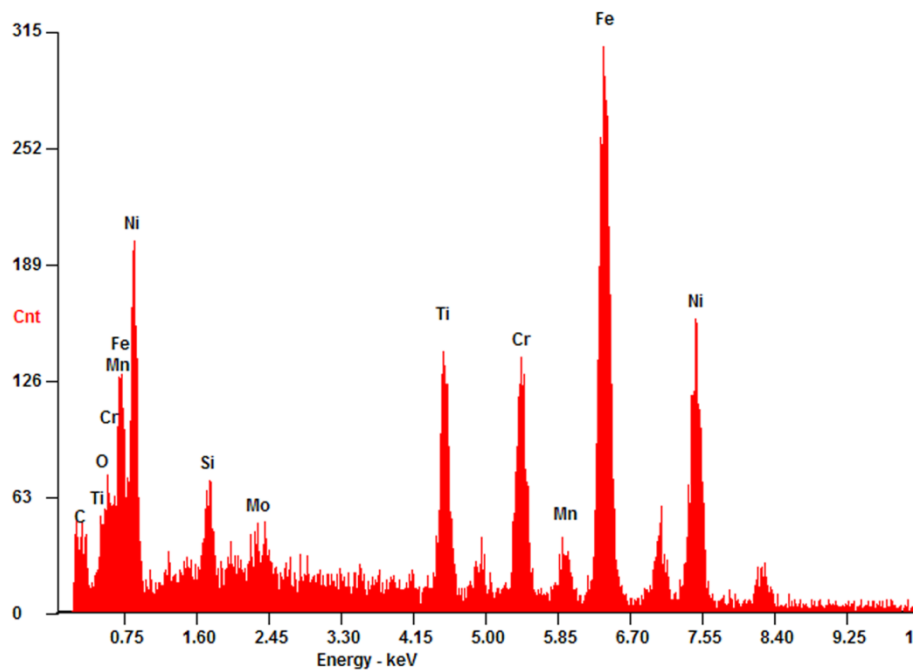

Fig. 11. EDX spectrum obtained from the interdendritic region indicated in Fig. 10.
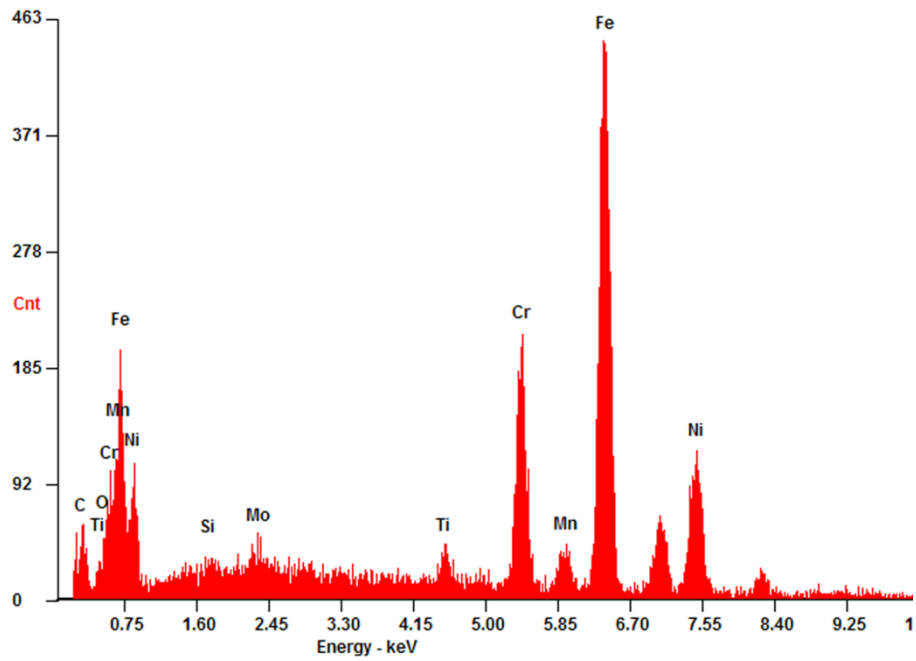
Fig. 12. EDX spectrum obtained from the dendrite core indicated in Fig. 10.

Table 3. Chemical composition (wt%) of interdendritic region determined by EDX (see Figs. 10 and 11) and partition coefficient k_{IDR}.

Element	wt%	k_{IDR}
Ti	9.22	4.01
Cr	11.80	0.79
Fe	41.77	0.77
Ni	31.00	1.25

Table 4. Chemical composition (wt%) of dendrite core determined by EDX (see Figs. 10 and 12) and partition coefficient k_{DC}.

Element	wt%	k_{IDR}
Ti	1.95	0.85
Cr	15.05	1.005
Fe	55.62	1.02
Ni	22.45	0.91

12

The segregation of Ni and Ti towards the interdendritic region [18] of the weld nugget explains the different formation kinetics of γ' and η precipitates (Ni and Ti-rich phases) in the weld nugget with respect to that observed in the base metal. The enrichment in Ni and Ti of the interdendritic region causes the development of γ'-free zones in the dendrite core of the weld nugget (Fig. 13), which contrasts with the base metal where the γ' precipitates are homogeneously distributed within the grain (Fig. 14). On the other hand, the growth kinetics of the γ' precipitates is faster in the weld nugget, where the γ' phase is clearly observable from an aging time of 50 h (Fig. 13), than in the base metal, where the γ' phase is clearly observable from an aging time of 200 h (Fig. 14); this result is consistent with that of Yan et al. [51], who found that the growth of γ' precipitates in the weld metal, where the diffusivity of γ' forming elements is higher than in the base metal due to the higher concentration of vacancies, is faster than in the base metal. The faster growth kinetics of the γ' precipitates gives rise to a more pronounced depletion of Ni and Ti, which, in turn, causes that the η phase appears later (with longer aging times) in the weld nugget, where the η phase is clearly observable from an aging time of 50 h, than in the base metal, where the η phase is clearly observable from an aging time of 25 h.
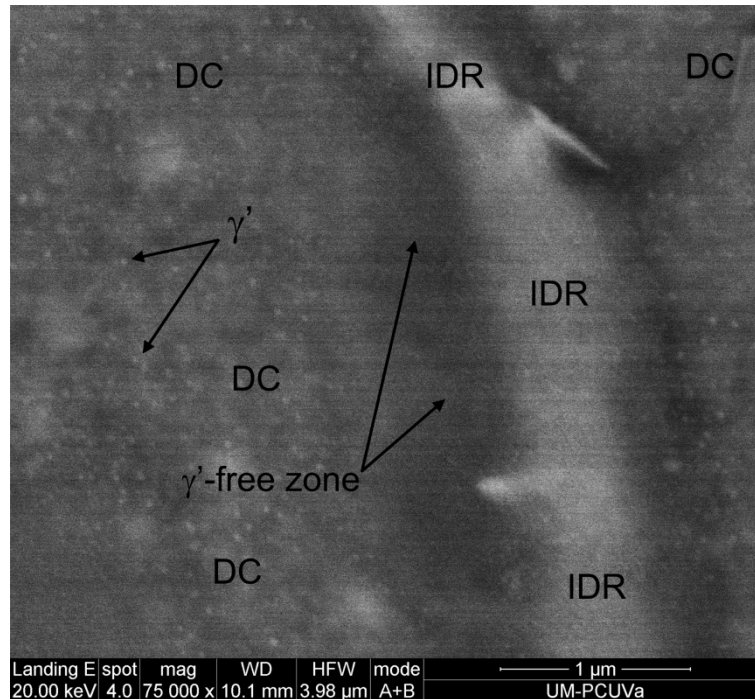

Fig. 13. SEM micrograph of the weld nugget of the specimen No. 4. The figure shows the γ' phase and the zone of the dendrite core (DC) that is adjacent to the interdendritic region (IDR) and that is a γ'-free zone because the interdendritic region is enriched in Ni and Ti. Electrolytic etching with etchant No. 83 according to ASTM E407-07 [40].
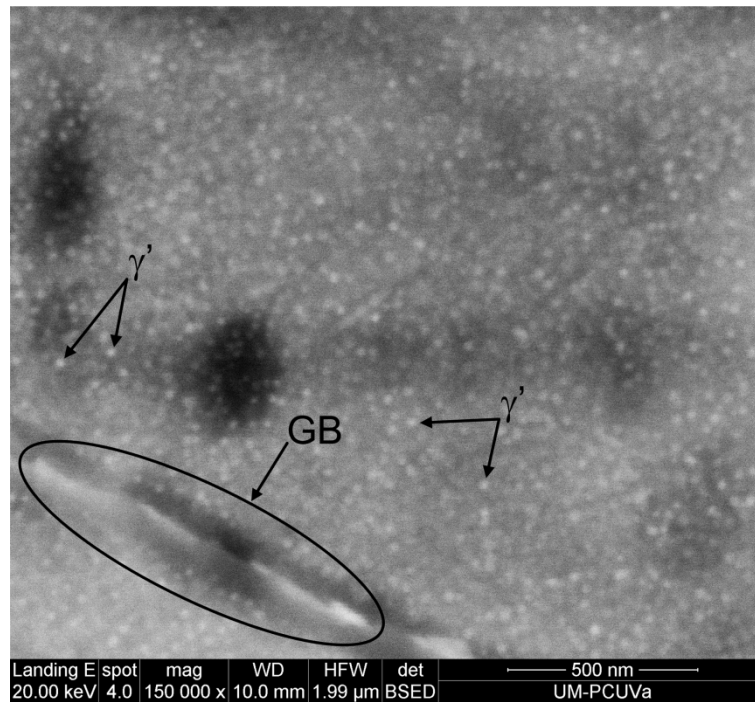
Fig. 14. SEM micrograph of the base metal of the specimen No. 6. The figure shows the grain boundary (GB) and how the γ' precipitates are homogeneously distributed within the grain. Electrolytic etching with etchant No. 83 according to ASTM E407-07 [40].

4 Conclusions

The present work aims to study of the combined effect of RSW and precipitation hardening on the localized corrosion of A286 superalloy by using DLEPR test. The major conclusions are:

1. For both the base metal and the weld nugget, the maximum localized corrosion is reached at the aging time from which the η phase is clearly observable: at 25 h for the base metal and at 50 h for the weld nugget.
2. The localized corrosion for the entire specimen: (i) takes an intermediate value between those of the base metal and weld nugget; and (ii) reaches its highest values at the aging times from which the η phase is clearly observable in the base metal (25 h) and in the weld nugget (50 h).
3. Both in the base metal and in the weld nugget, before the η phase is clearly observable, the localized corrosion increases as the aging time increases, i.e., as γ' precipitates grow.
4. The complex effect of η phase on the localized corrosion may be explained by the fact that the η phase precipitation at grain boundary promotes the localized corrosion at grain boundary on the one hand, whilst on the other, the η phase indirectly improves the localized corrosion resistance because it grows at the expense of γ' phase.
5. The fact that the localized corrosion resistance of the weld nugget is different from that shown by the base metal may be explained by the segregation of Ni and Ti towards the interdendritic region of the weld nugget, which justifies the different formation kinetics of

γ′ and η precipitates (Ni and Ti-rich phases) in the weld nugget with respect to that observed in the base metal.

6. The enrichment in Ni and Ti of the interdendritic region causes the development of γ′-free zones in the dendrite core of the weld nugget which contrasts with the base metal where the γ′ precipitates are homogeneously distributed within the grain.

7. The growth kinetics of the γ′ precipitates is faster in the weld nugget than in the base metal, which gives rise to a more pronounced depletion of Ni and Ti, which, in turn, causes that the η phase appears later (with longer aging times) in the weld nugget than in the base metal.

References

[1]   Mustafa AH, Hashmi MS, Yilbas BS, et al. Investigation into thermal stresses in gas turbine transition-piece: Influence of material properties on stress levels. J. Mater. Process. Technol. 2008;201:369–373.

[2]   Mouritz AP. Introduction to Aerospace Materials. Cambridge, UK: Woodhead Publishing Limited; 2012.

[3]   Narayana Rao M. High performance stainless steels for critical engineering applications. Trans. Indian Inst. Met. 2010;63:321–330.

[4]   Savoie M, Esnouf C, Fournier L, et al. Influence of ageing heat treatment on alloy A-286 microstructure and stress corrosion cracking behaviour in PWR primary water. J. Nucl. Mater. 2007;360:222–230.

[5]   Fournier L, Savoie M, Delafosse D. Influence of localized deformation on A-286 austenitic stainless steel stress corrosion cracking in PWR primary water. J. Nucl. Mater. 2007;366:187–197.

[6]   Krishna SC, Gangwar NK, Jha AK, et al. On the direct aging of iron based superalloy hot rolled plates. Mater. Sci. Eng. A. 2015;648:274–279.

[7]   Singhal LK, Martin JW. The mechanism of tensile yield in an age-hardened steel containing γ′ (ordered Ni3Ti) precipitates. Acta Metall. 1968;16:947–953.

[8]   Thompson AW, Brooks JA. The mechanism of precipitation strengthening in an iron-base superalloy. Acta Metall. 1982;30:2197–2203.

[9]   Zhang P, Zhu Q, Hu C, et al. Cyclic deformation behavior of a nickel-base superalloy under fatigue loading. Mater. Des. 2015;69:12–21.

[10]   Zhao MJ, Guo ZF, Liang H, et al. Effect of boron on the microstructure, mechanical properties and hydrogen performance in a modified A286. Mater. Sci. Eng. A. 2010;527:5844–5851.

[11]   Seifollahi M, Razavi SH, Kheirandish S, et al. The Mechanism of η Phase Precipitation in A286 Superalloy During Heat Treatment. J. Mater. Eng. Perform. 2013;22:3063–3069.

[12]   Li X, Zhang J, Rong L, et al. Cellular η phase precipitation and its effect on the tensile properties in an Fe-Ni-Cr alloy. Mater. Sci. Eng. A. 2008;488:547–553.

[13]   Barlow CY, Ralph B. Observations of cellular transformation products in nickel-base superalloys. J. Mater. Sci. 1979;14:2500–2508.

[14]   De Cicco H, Luppo MI, Gribaudo LM, et al. Microstructural development and creep behavior in A286 superalloy. Mater. Charact. 2004;52:85–92.

[15]   Brooks JA, Thompson AW. Microstructure and hydrogen effects on fracture in the alloy A-286. Metall. Trans. A. 1993;24:1983–1991.

[16]   Guo Z, Liang H, Zhao M, et al. Effect of boron addition on hydrogen embrittlement sensitivity in Fe-Ni based alloys. Mater. Sci. Eng. A. 2010;527:6620–6625.

[17]   Rho BS, Nam SW, Xie X. The effect of test temperature on the intergranular cracking of Nb-A286 alloy in low cycle fatigue. J. Mater. Sci. 2002;37:203–209.

[18]   Chen S, Zhao M, Rong L. Effect of Ti content on the microstructure and mechanical properties of electron beam welds in Fe-Ni based alloys. Mater. Sci. Eng. A. 2013;571:33–37.

[19]   Martín Ó, De Tiedra P, San-Juan M. Combined effect of resistance spot welding and precipitation hardening on tensile shear load bearing capacity of A286 superalloy. Mater. Sci. Eng. A. 2017;688:309–314.

[20]   ASM International Handbook Committee. Welding. In: Davies JR, editor. ASM Spec. handbook. Stainl. steels. Materials Park, OH: ASM International; 1994. p. 340–401.

[21] Brooks JA, Krenzer RW. Progress toward a more weldable A-286. Weld. J. 1974;53:242S – 245S.

[22] Shinozaki K. Welding and joining Fe and Ni-base superalloys. Weld. Int. 2001;15:593–610.

[23] Martín O, López M, Martín F. Redes neuronales artificiales para la predicción de la calidad en soldadura por resistencia por puntos. Rev. Metal. 2006;42:345–353.

[24] Eftekharimilani P, van der Aa EM, Hermans MJM, et al. Microstructural characterisation of double pulse resistance spot welded advanced high strength steel. Sci. Technol. Weld. Join. 2017;22:545–554.

[25] Martín Ó, López M, De Tiedra P, et al. Prediction of magnetic interference from resistance spot welding processes on implantable cardioverter-defibrillators. J. Mater. Process. Technol. 2008;206:256–262.

[26] Martín Ó, Pereda M, Santos JI, et al. Assessment of resistance spot welding quality based on ultrasonic testing and tree-based techniques. J. Mater. Process. Technol. 2014;214:2478–2487.

[27] Kianersi D, Mostafaei A, Mohammadi J. Effect of welding current and time on the microstructure, mechanical characterizations, and fracture studies of resistance spot welding joints of AISI 316L austenitic stainless steel. Metall. Mater. Trans. A Phys. Metall. Mater. Sci. 2014;45:4423–4442.

[28] Pouranvari M, Alizadeh-Sh M, Marashi SPH. Welding metallurgy of stainless steels during resistance spot welding Part I: fusion zone. Sci. Technol. Weld. Join. 2015;20:502–511.

[29] Hoppin GS, Yount RE. Fusion Welding of Age-Hardenable Superalloys. SAE Tech. Pap. 1969;690102.

[30] De Tiedra P, Martín Ó, San-Juan M. Potentiodynamic study of the influence of gamma prime and eta phases on pitting corrosion of A286 superalloy. J. Alloys Compd. 2016;673:231–236.

[31] Martín Ó, De Tiedra P, San-Juan M. Study of influence of gamma prime and eta phases on corrosion behaviour of A286 superalloy by using electrochemical potentiokinetic techniques. Mater. Des. 2015;87:266–271.

[32] Ahedo V, Martín Ó, Santos JI, et al. Independence of EPR and PAP tests performed on resistance spot welding joints. Corros. Eng. Sci. Technol. 2017;1–7.

[33] Pereda M, Santos JI, Martín Ó, et al. Direct quality prediction in resistance spot welding process: Sensitivity, specificity and predictive accuracy comparative analysis. Sci. Technol. Weld. Join. 2015;20:679–685.

[34] Prohaska M, Kanduth H, Mori G, et al. On the substitution of conventional corrosion tests by an electrochemical potentiokinetic reactivation test. Corros. Sci. 2010;52:1582–1592.

[35] De Tiedra P, Martín Ó, López M. Combined effect of resistance spot welding and post-welding sensitization on the degree of sensitization of AISI 304 stainless steel. Corros. Sci. 2011;53:2670–2675.

[36] Garcia C, de Tiedra MP, Blanco Y, et al. Intergranular corrosion of welded joints of austenitic stainless steels studied by using an electrochemical minicell. Corros. Sci. 2008;50:2390–2397.

[37] Kumar S, Shahi AS. Studies on metallurgical and impact toughness behavior of variably sensitized weld metal and heat affected zone of AISI 304L welds. Mater. Des. 2016;89:399–412.

[38] García C, Martín F, Blanco Y, et al. Corrosion behaviour of duplex stainless steels sintered in nitrogen. Corros. Sci. 2009;51:76–86.

[39] García C, Martín F, de Tiedra P, et al. Electrochemical reactivation methods applied to PM austenitic stainless steels sintered in nitrogen–hydrogen atmosphere. Corros. Sci. 2008;50:687–697.

[40] ASTM E407-07e1. Standard Practice for Microetching Metals and Alloys. 2007.

[41] McCauley RB, Bennett MP, Bodary WD, et al. Resistance Spot Welding. In: Lyman T, editor. Met. Handbook. Vol. 6 Weld. Brazing. 8th ed. Metals Park, OH: American Society for Metals; 1971. p. 401–424.

[42] Aslanlar S. The effect of nucleus size on mechanical properties in electrical resistance spot welding of sheets used in automotive industry. Mater. Des. 2006;27:125–131.

[43]   Bose A, De PK. An EPR Study on the Influence of Prior Cold Work on the Degree of Sensitization of AISI 304 Stainless Steel. CORROSION. 1987;43:624–631.

[44]   Reclaru L, Lerf R, Eschler PY, et al. Corrosion behavior of a welded stainless-steel orthopedic implant. Biomaterials. 2001;22:269–279.

[45]   Alizadeh-Sh M, Pouranvari M, Marashi SPH. Welding metallurgy of stainless steels during resistance spot welding Part II –heat affected zone and mechanical performance. Sci. Technol. Weld. Join. 2015;20:512–521.

[46]   Číhal V, Štefec R. On the development of the electrochemical potentiokinetic method. Electrochim. Acta. 2001;46:3867–3877.

[47]   Shingledecker JP, Evans ND, Pharr GM. Influences of composition and grain size on creep-rupture behavior of Inconel® alloy 740. Mater. Sci. Eng. A. 2013;578:277–286.

[48]   Zhong Z, Gu Y, Yuan Y. Microstructural stability and mechanical properties of a newly developed Ni-Fe-base superalloy. Mater. Sci. Eng. A. 2015;622:101–107.

[49]   Zhao J-C, Ravikumar V, Beltran AM. Phase precipitation and phase stability in nimonic 263. Metall. Mater. Trans. A. 2001;32A:1271–1282.

[50]   Zhao S, Xie X, Smith GD, et al. Research and Improvement on structure stability and corrosion resistance of nickel-base superalloy INCONEL alloy 740. Mater. Des. 2006;27:1120–1127.

[51]   Yan Y, Yan Y, He Y, et al. The mechanism of precipitation strengthening in Fe–Ni austenitic alloy electron beam weldment. Mater. Sci. Eng. A. 2015;630:85–89.